An improved streamline curvature-based design approach for transonic axial-flow compressor blading

Hasani Azamar, Vassilios Pachidis
h.azamaraguirre@cranfield.acuk
Cranfield University
Centre for Propulsion
Cranfield
United Kingdom

Ioannis Templalexis
Hellenic Air Force Academy
Department of Aeronautical Sciences
Athens
Greece

ABSTRACT

The increasing demand to obtain more accurate turbomachinery blading performance in the design and analysis process has led to the development of higher fidelity flow field models. Despite extensive flow field information can be collected from three-dimensional (3-D) Reynolds-averaged Navier-Stokes (RANS) numerical simulations; it comes at a high computational cost in terms of time and resources, particularly if a comprehensive design space is explored during optimization. In contrast, through-flow methods such as streamline curvature (SLC), provide a flow solution in minutes whilst offering acceptable results. Furthermore, if the SLC fidelity is improved, a more detailed component-blading study is expected.

For this reason, a fully-detailed transonic flow framework was implemented and validated in an existing in-house two-dimensional (2-D) SLC compressor performance to improve the performance results fidelity in transonic conditions. The improvements consist of two sections: (1) blade-profile modelling; (2) flow field solution. The blade-profile modelling considers a 3-D blade-element-layout method to correctly model the sweep and lean angle, which determine the shock structure.

The essential part of the transonic flow framework is its solution, formed of two parts: (1) a physics-based shock-wave model to predict its structure, and associated losses; (2) and a novel choking model to define the choke level for future spanwise mass flow redistribution. To demonstrate the functionality of the full comprehensive transonic-flow approach, the well-known NASA Rotor 67 compressor was used to prove that the inlet relative flow angle should be limited by the choking incidence at the required blade span locations. A 3-D RANS numerical simulation for the NASA Rotor 67 validated the transonic-flow model, showing minimum differences in the spanwise mass flow distribution for the choked off-design cases. The current improvements implemented in the 2-D SLC compressor/fan performance simulator enhance the fidelity not only in analysis mode, but also in design optimisation applications.

Keywords: Fan; Compressor; Blade; Streamline Curvature; Shock Waves; Shock Losses; Choking/

NOMENCLATURE

0-D	Zero-Dimensional
2-D	Two-Dimensional
3-D	Three-Dimensional
CFD	Computational Fluid Dynamics
IGV	Inlet Guide Vane
MCA	Multiple-Circular Arc
NACA	National Advisory Committee for Aeronautics
OGV	Outlet Guide Vane
RANS	Reynolds-Averaged Navier-Stokes
REE	Radial Equilibrium Equation
SLC	Streamline Curvature
SOCRATES	Synthesis of Correlations for the Robust Assessment of Turbomachinery Engine Systems
SWBLI	Shock-Wave and Boundary-Layer Interaction

Symbols

Latin

A	Area, Contraction ratio
a	Speed of sound
C	Turning Rate
d	Detachment distance
E	Error function
h	Hub, Distance between stagnation streamline position and bow-wave vertex
k	Blade angle
L	Distance between sonic point of hyperbola index
M	Mach number
m	Mass
N	Number of integration points
P	Total pressure
p	Static pressure
ps	Pressure surface
R	Ray coordinate in conical system, Gas constant
r	Radial coordinate in cylindrical system
S	Blade profile path, Shock angle
s	Blade profile surface, Spacing or pitch
sp	Stacking points
ss	Suction surface
T	Temperature
U	Blade speed
u	Flow velocity
V	Relative velocity
x	Flow direction, Radial coordinate in Cartesian system
y	Tangential coordinate in Cartesian system
z	Axial coordinate in Cartesian and cylindrical system

Greek

Λ	Mass flow choking coefficient
Π	Total pressure ratio
Υ	Hyperbola co-vertex
Ψ	Non-dimensional transition point handle
Δy	Increment in y direction
α	Absolute flow angle, Streamline cone angle
β	Flow angle

γ	Specific ratio
δ	Deflection angle
ϵ	Angle coordinate in conical system
η	Lean angle
ι	Incidence
λ	Sweep angle, Choking margin
μ	Mach angle
ν	Prandtl-Meyer angle
χ	Hyperbola ratio
ω	Rotational speed
ϖ	Loss coefficient

Subscripts

0	Absolute
1	Inlet state
2	Outlet state
A	Point A on suction surface
a	Speed of sound
B	Intersection between stagnation streamline and bow-wave vertex
bow	Bow wave
c	Camberline, Centroid of mass
C	Absolute velocity
ch	Choke
d	Immediately behind the bow shock
E	First-captured wave
i	Counter
in	Inlet
LE	Leading edge
m	Meridional
max	Maximum
min	Minimum
n	Any point
ns	Normal shock
nst	Negative stall
o	Centre
out	Outlet
ps	Passage shock
rel	Relative
s	Sonic point
SB	Intersection between sonic line and blade-profile leading edge
sh	Total shock
ss	Suction surface
st	Stall
St	Stream tube
t	Transition point
uch	unchoke

Superscripts

*	Critical, Design
.	Flow rate
-	Mass averaged
~	Obtained from assumed value
'	Relative

1.0 INTRODUCTION

Aircraft gas-turbine engine design and analysis is still a pleasant art to be further explored. The demand of advanced-design transonic axial-flow fans or compressors in both, commercial and military aircraft engines has expanded. Inasmuch as modern aero gas-turbine engines, especially turbofans, are required to be light and compact, transonic compressing systems fit the purpose due the high single-stage pressure ratio provided with isentropic efficiencies still well above 85%.

Accurate and robust fan and compressor flow field prediction remains elusive [1]. Off-design performance estimation still to be a challenge for conventional simulation tools, which show significant deviation against real behaviour [2]. Even though computational fluid dynamics (CFD) plays an essential role in the turbomachinery design than it does in any other fluid-related field [3], there are still limitations in turbulence and transition, particularly for off-design cases [1]. Turbomachinery CFD analysis is three dimensional (3-D) and numerically solve the viscosity effects at a small scale, however, it is not an exact science [4]. Additionally, CFD simulations come at high computational costs in terms of solution time and memory, complexity to obtain the required initial and boundary conditions, and lack of flexibility to incorporate or even modify any loss or deviation model [2,5–7].

Alternatively, through-flow methods provide fast and acceptable solution at low cost in terms of computational run-time and resources [2,6–8]. Since the development of turbomachinery through-flow codes in the late forties and fifties, streamline curvature (SLC) [9] and stream function or matrix methods [10] have evolved. Among the through-flow techniques, SLC is the most typically used numerical method for turbomachinery design and analysis [1,3] representing the backbone for the design process [11] due to economical and practical reasons [12]. Flow in SLC is assumed to be two dimensional (2-D), compressible, inviscid, and steady. In fact, a fully detailed analysis for an isolated gas-turbine engine component can be obtained through SLC methods. In contrast to CFD, SLC is flexible to incorporate empiricism in the form of loss and deviation models. Besides, SLC simulations require less time to set up the model and the initial and boundary conditions than in CFD. If design optimisation is intended, SLC techniques are the most suitable to avoid the intolerably high computational times of CFD [12]. Furthermore, 2-D SLC component analyses can be coupled with a low-fidelity zero-dimensional (0-D) solver for the entire engine, known as component zooming [13–17]. Through this amalgamation, influence of high-fidelity analysed components is incorporated into the low-fidelity engine-cycle performance.

Given the importance of the SLC methods, the fidelity of an existing in-house 2-D axial-flow fan/compressor simulation code, SOCRATES (Synthesis of correlations for the robust assessment of turbomachinery engine systems) [2,5,18], was improved to have an enhanced handling of transonic flow in the analysis and design process. Transonic flow analysis in compressors and fans is complex due to the resulting highly three-dimensional (3-D) flow field, shock waves, their interaction with the endwall and blade boundary layer (SWBLI), spanwise mixing, and tip clearance secondary flows [1]. In general, SLC computer programs lack of robustness to handle transonic and supersonic flows [11] and their use in transonic compressors has been limited [1].

In recent years, emphasis has been placed to develop flow-physics-based models instead of fully and semi- empirical aerodynamic correlations in the SLC simulations [19]. For these reasons, a comprehensive transonic flow framework was devised, implemented, and validated in the 2-D SLC software. The transonic flow framework consists of two sections: (1) blade-profile modelling; (2) flow field solution. In the blade-profile modelling, a 3-D blade-element-layout method [20,21] was implemented to represent the sweep and lean angle, as they interact with the radially swept shock [22], affecting the radial equilibrium, and thence, redistributing the inlet and outlet velocities [23]. The core of the transonic flow framework is its solution, formed of two parts: (1) a physics-based shock-wave model to predict its structure [24–27], and associated losses [28–31]; (2) a novel choked-flow treatment model to estimate choking evolution.

2.0 METHODOLOGY

To account for a higher-fidelity flow field prediction in transonic axial-flow compressors, a 2-D SLC code [2,5,18] was improved to include a 3-D blade-element-layout method for sweep and lean angles, a shock-wave structure and loss model, and a novel choking-evolution model.

2.1 3-D Blade-Element-Layout Method

Compressor blade-profile section modelling was based on the constant-turning blade-element-layout method defined by Crouse *et al.* (1969) [20]. Each blade-profile section is conveniently projected on a conical surface, which approximatse the axisymmetric stream surface. Flow across the blades is influenced by several interacting forces; however, the driving factor for the local flow is the surface curvature, which can be represented by the rate of change-of-surface-angle with respect to the streamline. The present blade-element-layout method maintains a constant rate of angle change with respect to the path distance at every defined arc segment of the camberline, suction surface and pressure surface. This method is suitable to model multiple-circular-arc (MCA) –type blade profile, widely found in transonic compressors to regulate chordwise the flow turning to control the shock-wave at the throat area.

The rate of change of blade angle κ with respect to the blade profile path S is defined by a constant turning rate C,

$$\frac{dk}{dS} = -C \tag{1}$$

Having the corresponding camberline blade angles k_c at the leading edge, transition point, and trailing edge, and following Eq. 1, the camberline is laid out in the conical system obtaining the R-ϵ coordinates. Suction and pressure surface coordinates in the conical system are computed from the calculated camberline by adding the corresponding thicknesses normal to a tangent of the camberline and following Eq. 1.

The 3-D blade shaping consists in sweeping and/or leaning each blade profile section by a constant or compound sweep λ or lean angle η with respect of the stacking axis. As the stacking axis passes through the stacking points sp which are located in the blade surface centre-of-areas, the stacking point coordinates are obtained in the conical coordinate system as

$$R_{sp} = \frac{\int R\,dA}{\int dA} \tag{2}$$

$$\varepsilon_{sp} = \frac{\int \varepsilon\,dA}{\int dA} \tag{3}$$

Which can be solved through numerical integration.

Having the R-ϵ coordinates for the blade profile stacking points, a translation to cylindrical system is performed as follows. The stacking point radial coordinate is simply a trigonometric function of the cone angle α,

$$r_{sp} = R_{sp}sin\alpha \tag{4}$$

$$z_{sp} = R_{sp_h}cos\alpha_h + \left(r_{sp} - R_{sp_h}sin\alpha_h\right)tan\lambda \tag{5}$$

Upon the stacking point displacement in the circumferential direction, the lean angle causes a tangential deflection δ, which is

$$\delta = arcsin\left\{\frac{r_{sp_h}}{r_{sp}}(\frac{tan\eta}{1+tan^2\eta}\left[\sqrt{\left(\frac{r_{sp}}{r_{sp_h}}\right)^2(1+tan^2\eta) - tan^2\eta} - 1\right]\right\} \tag{6}$$

Hence, the stacking point θ-coordinate with the lean-angle tangential deflection is

$$\theta_{sp} = \theta_{sp_h} = \frac{\varepsilon_{sp_h}}{sin\alpha_h} + \delta \tag{7}$$

Finally, the x-y-z blade coordinates for the blade elements can be computed with the following relationship between Cartesian and cylindrical system:

$$x = Rsin\alpha cos(\frac{\varepsilon}{sina} + \theta_{sp_h} + \delta - \frac{\varepsilon_{sp}}{sina} - \theta_{sp_h}) \tag{8}$$

$$y = Rsin\alpha \sin\left(\frac{\varepsilon}{sina} + \theta_{sp_h} + \delta - \frac{\varepsilon_{sp}}{sina} - \theta_{sp_h}\right) \tag{9}$$

$$z = z_{sp} - (R_{sp} - R)cos\alpha \tag{10}$$

2.2   Shock-wave Structure and Loss Model

A physics-based shock- structure and loss model was developed and implemented into the 2-D SLC axial-flow fan/compressor performance simulation software [2,5,18]. The shock model works in two parts: through the prediction of the bow wave structure [24,27] and loss [26], and the iterative solution of the passage shock location [1,28,29,31] and its corresponding losses [25].

2.2.1   Bow Wave
The bow wave is a detached shock wave from the blade blunt leading edge. The analytical bow-wave structure in terms of shape and location was based on the hyperbola approximation reported by Moeckel [24], as observed in Fig. 1.
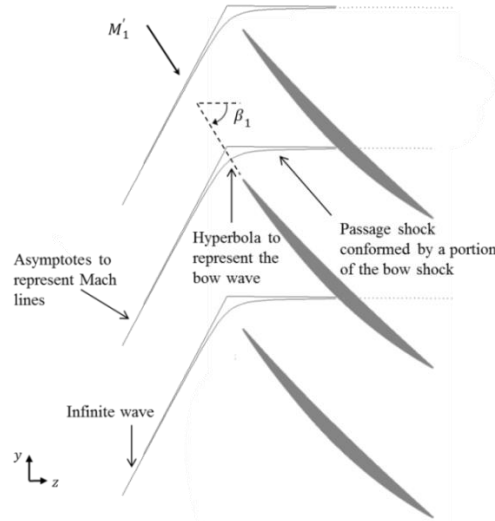

Figure 1 Hyperbolic representation for a bow shock in a blade cascade.

This shock-structure model approach relies on 2 fundamental assumptions: (1) The detached shock is assumed to be hyperbolic and asymptotic to the free-stream Mach wave. (2) The sonic line that divides the pocket of subsonic flow and the outer supersonic flow is considered to be straight at an angle that depends on the inlet Mach number.

The bow-wave hyperbolic approximation [24] calculates the parameters shown in Fig. 2, required to obtain the relative total-pressure ratio behind the inlet and immediately behind the bow wave at the sonic point. Forasmuch as the detached shock is normal to the incoming flow, the hyperbola-shape bow wave is assumed to lie on a local frame of reference aligned to the flow. In consequence, the overall shock-system model is rotated by an angle β_1 around the hyperbola centre, which is the intersection point of its asymptotes. Hence, the hyperbola centre and vertex are situated at $y'_o = 0$ and $y'_v = 0$, respectively, on the relative frame of reference. For convenience all the shock structure calculations ae performed in a local coordinate system aligned with the inlet flow with z'-axis origin at $z'_o = 0$.

Figure 2 Hyperbolic approximation for a bow wave ahead of a blade-profile leading edge.

The central part of a detached shock gives a strong shock solution, while farther out the shock is considered to be weak. The shock angle that corresponds for a detached wave at the central part of the hyperbola-shape bow wave is

$$\varsigma_{detach} = \frac{1}{2}\text{acos}\left\{\frac{1}{\gamma}\left[\frac{\gamma+1}{2} - \cos 2\mu \right.\right.$$

$$\left.\left. - \sqrt{\gamma+1}\sqrt{\left(\frac{\gamma+1}{2} - \cos 2\mu\right)^2 + \frac{\gamma(3-\gamma)}{4}}\right]\right\} \tag{11}$$

For detached shock analysis, a wedge is assumed with origin at the hyperbola vertex and tangent to the blade-profile leading edge circle with radius r_{LE}. The wedge-half angle δ is the maximum deflection angle to detach the bow shock. Yet, to guarantee that the bow wave is fully detached, the wedge half-angle is assumed to be the detachment deflection plus one degree:

$$\delta = \delta_{detach} + 1° \tag{12}$$

Where the maximum deflection angle for which an oblique shock becomes detached is

$$\delta_{detach} = \text{atan}\left\{\tan\varsigma_{detach}\left[\frac{(\gamma+1)M_1'^2}{2(M_1'^2\sin^2\varsigma_{detach} - 1)} - 1\right]\right\}^{-1} \tag{13}$$

The intersection between the wedge and leading edge gives the sonic point SB. A normal line to the tangent at point SB forms the sonic line. The sonic line in set with the bow wave central part bounds the region to contain the subsonic flow, whereupon the sonic line represents the border for which the flow becomes sonic.

The y'-axis distance between the bow-wave vertex and the point SB is calculated as

$$y_{SB} = \cos\delta = \cos(\delta_{detach} + 1°) \tag{14}$$

The intersection between the sonic line and the bow wave gives the sonic point S. Similarly as in the case of detached-wave strong portion, the shock angle at point S for which the downstream flow becomes sonic is determined by

$$\varsigma_s = \text{asin}\sqrt{\frac{1}{2\gamma}\left[\frac{\gamma-3}{2}\sin^2\mu + \frac{\gamma+1}{2} + \sqrt{4\gamma\sin^4\mu + \left(\frac{\gamma-3}{2}\sin^2\mu + \frac{\gamma+1}{2}\right)^2}\right]} \tag{15}$$

Therefore, the deflection angle at point S becomes

$$\delta_s = \text{atan} \left\{ \tan \varsigma_s \left[\frac{(\gamma + 1)M_1'^2}{2(M_1'^2 \sin^2 \varsigma_s - 1)} - 1 \right] \right\}^{-1} \tag{16}$$

And the shock angle at the sonic line centroid of mass c is computed as

$$\varsigma_c = \text{atan} \sqrt{\frac{4(M_1'^2 - 1) \text{atan}^2 \varsigma_s - 3}{M_1'^2 - 1}} \tag{17}$$

The distance between the axial axis in the relative frame of reference and point S is determined through the continuity relation for the flow that passes the sonic line. Inasmuch as the total temperature and total pressure are constant along every streamline downstream of the bow shock, the simplified version of the continuity can be written as

$$y_S = y_{SB} \frac{1}{1 - \Pi_{d1_C}'^{-1} \cos \eta \, A} \tag{18}$$

Where Π_{d1_C}' is the relative total-pressure ratio between the inlet (state 1) and immediately behind the bow wave (state d) at the sonic point, given by [27]

$$\Pi_{d1_C}' = \frac{P_d'}{P_1'} = \left[\frac{(\gamma + 1)M_1'^2 \sin^2 \varsigma_c}{(\gamma - 1)M_1'^2 \sin^2 \varsigma_c + 2} \right]^{\frac{\gamma}{\gamma - 1}} \left[\frac{(\gamma + 1)}{2\gamma M_1'^2 \sin^2 \varsigma_c - (\gamma - 1)} \right]^{\frac{1}{\gamma - 1}} \tag{19}$$

η is the angle between the sonic line and the y'-axis and is the arithmetic mean between the two line extremity angles: the wedge half-angle or deflection angle to detach the shock and the deflection angle at the sonic point; this is

$$\eta = \frac{1}{2}(\delta + \delta_s) = (\delta_{detach} + 1° + \delta_s) \tag{20}$$

And A represents the area contraction ratio to isentropically decelerate the supersonic free stream to sonic conditions between the critical area and the actual area,

$$A = \frac{A^*}{A} = \left\{ \frac{1}{M_1'} \left[\frac{2}{\gamma + 1} \left(1 + \frac{\gamma - 1}{2} M_1'^2 \right) \right]^{\frac{\gamma + 1}{2(\gamma - 1)}} \right\}^{-1} \tag{21}$$

Whereupon, the bow-wave equation in the relative frame can be written as

$$\frac{z_{bow}'^2}{y_S^2 \left[(M_1'^2 - 1)^2 \tan^2 \varsigma_s - (M_1'^2 - 1) \right]}$$
$$- \frac{y_{bow}'^2}{y_S^2 \tan \mu \left[(M_1'^2 - 1)^2 \tan^2 \varsigma_s - (M_1'^2 - 1) \right]} = 1 \tag{22}$$

As not all the blade span experiences inlet relative supersonic flow, the bow-wave model was properly setup to identify where bow-wave structures are needed as shown in Fig. 3.
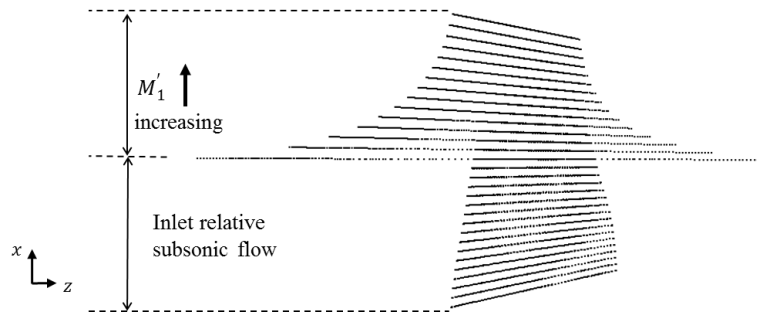

Figure 3 Bow-wave prediction in the meridional plane for the 2-D SLC compressor simulator.

Naturally, as the inlet relative Mach number increases from the first streamline to have supersonic flow to the tip, the detachment distance reduces and the Mach angle lowers, yet increasing the obliquity of the bow wave, as seen in Fig. 4. Hence, as the span is

reduced and $M_1' \geq 1$, the bow-wave structure in set with the Mach lines becomes wider and more open, tending to become normal.
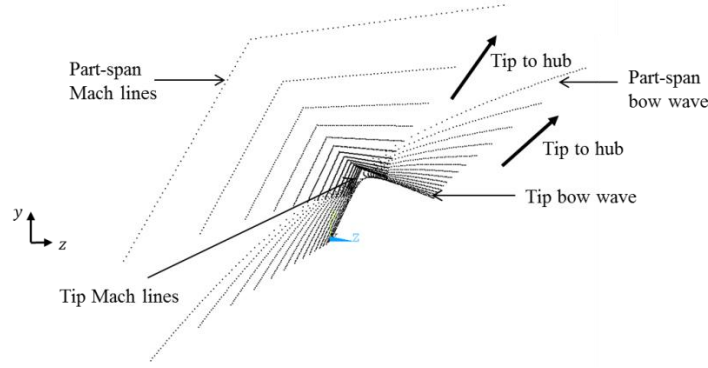

Figure 4 Bow-wave structures prediction in the blade-to-blade plane for the 2-D SLC compressor simulator.

2.2.2   Bow-Wave Losses

Along the bow wave the shock angle changes due to the hyperbola curvature. Thus, the shock angle for a detached wave at any point n in the y'-axis (perpendicular to the flow) is

$$\varsigma_n = \text{atan}\left(\frac{\sqrt{z_v'^2 + \left(M_1'^2 - 1\right)y}}{\left(M_1'^2 - 1\right)y}\right) \tag{23}$$

Therefore, the relative total-pressure recovery from Eq. 19 becomes Π_{d1}', by substituting ς_C for ς_n.

Eq. 23 demonstrates that every point on the bow wave produces a different relative total-pressure downstream of it. Therefore, an integration of infinitesimal P_d'/P_1' is required along the hyperbola, derived by Klapproth [32] and reported by Miller and Hartmann [27]. This formulation considers the distance in the distance h in the y'-axis distance from the bow-wave vertex to the real stagnation streamline position. Nevertheless, beyond the stagnation streamline on the opposite side of the passage shock, the losses are significantly smaller than in the strongest bow-wave portion [33], hence $h = 0$. In addition, the bow wave has its strongest part in its vertex, where the highest relative total-pressure decay is expected at $y' = 0$. For implementation purposes in a numerical code, the upper integration limit is defined as the sonic point s, as farther out beyond this point, the bow shock becomes weak, with negligible contribution to the overall bow-wave loss. Therefore, the infinitesimal integration of P_d'/P_1' along the bow-wave is simplified to

$$\Pi_{bow}' = \left(\frac{P_d'}{P_1'}\right)_{bow} = 1 - \frac{\int_0^s \left(1 - \frac{P_d'}{P_1'}\right) dy}{\int_0^s dy} \tag{24}$$

2.2.3   Passage Shock Wave

The passage shock is formed of two sections: a portion of the bow wave that penetrates into the passage, and a strong normal shock that stands on the suction surface of the adjacent suction surface as noted in Fig. 5. The point where the bow shock joins with the normal shock is the transition point t.
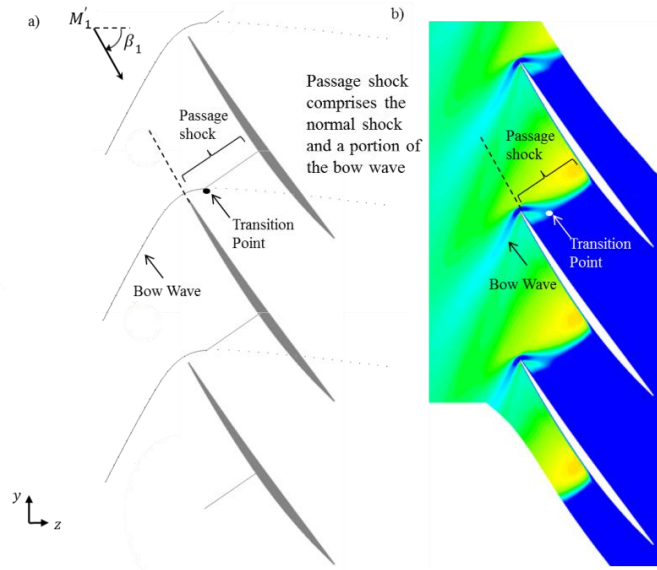
Figure 5 Transition point between the bow wave and the normal shock to form the passage
shock. a) 2-D SLC simulation. B) 3-D CFD simulation.

Transition point is obtained through an iterative approach to match the demanded outlet
static pressure. A non-dimensional distance ψ on the blade chord, between 0 and 1, is
assumed by the iterative scheme to obtain the transition point z_t'. A value of $\psi = 0$
accounts when $z_t' = z_v'$, for the case that the passage shock extends till the hyperbola
vertex. A value of $\psi = 1$ represents the scenario when the normal shock stands on the
adjacent blade trailing edge. For an assumed ψ, the transition point z'-axis location
becomes

$$z_t' = X' + \psi[X' + d' - s \sin \beta_1 + c \cos(\beta_1 - \xi) - z_v'] \qquad (25)$$

Thence, ψ controls the transition-point displacement as a function of the off-design
point as shown in Fig. 6 for highly-detached shock pattern and Fig. 7 for a more oblique
bow-wave structure.
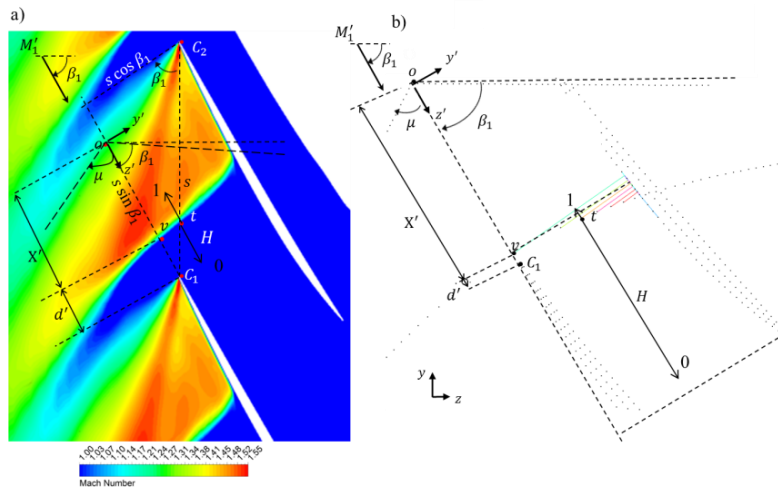
Figure 6 Highly-detached bow-wave at 89.1% span from hub to tip for the NASA Rotor 67 [34]
and 100% of design speed, at near-stall off-design condition, $\dot{m} = 29.21\ kg/s$, $p_{out} = 130\ kPa$.
a) 3-D CFD simulation. b) 2-D SLC simulation.
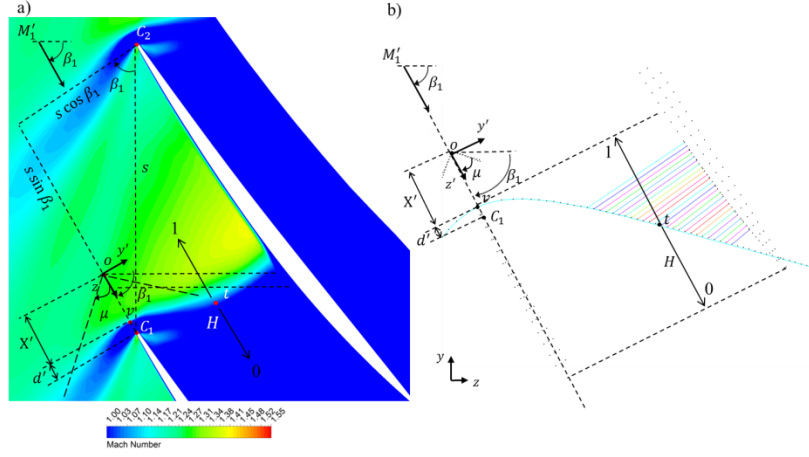
Figure 7 Highly-oblique bow-wave at 68.7% span from hub to tip for the NASA Rotor 67 [34] and 100% of design speed, at near-peak efficiency condition, $\dot{m} = 33.6\ kg/s$, $p_{out} = 122\ kPa$. a) 3-D CFD simulation. b) 2-D SLC simulation.

2.2.4 Passage-Shock Losses

As discussed before, the passage shock is formed by a bow-wave portion and a normal shock. Accordingly, the loss-integration procedure is divided for these two passage sections. The passage shock extends on a domain of length $s \cos \beta_1$, as is the d projected in the local frame of reference. Likewise to the bow-wave losses, an integration of losses along the passage domain is done, for which the spacing between equidistant integration points in the local frame of reference is defined as

$$\Delta y = \frac{s \cos \beta_1}{N} \qquad (26)$$

The integration domain for the passage bow-wave portion extends from $y'_{ps_0} = 0$ to $y'_{ps} = y_t{}'$. Every local radial coordinate is a summation of the previous point location and the spacing, specified as

$$\left(y'_{ps_i}\right)_{bow} = \sum_{i=1}^{n} \left(y'_{ps_{i-1}}\right)_{bow} + \Delta y \qquad (27)$$

Where n represents the last bow-wave integration point for which $y'_{ps_n} \leq y'_{ps}$. For every y'_{ps_i}, the hyperbola axial coordinate is obtained though the bow-wave equation derived in Eq. 22. The shock angle at every integration point on the hyperbola curvature can be obtained as in Eq. 23, giving

$$\varsigma_i = \operatorname{atan}\left(\frac{\sqrt{X'^2 + \left(M_1'^2 - 1\right)y'_{ps_i}}}{\left(M_1'^2 - 1\right)y'_{ps_i}}\right) \qquad (28)$$

In terms of the passage normal-shock, the integration domain lengths from $y'_{ps} = y_t{}'$ to $y'_{ps_N} = s \cos \beta_1$. Similar to Eq. 27, every integration point axial location is found in the local frame of reference as a summation of the precedent point location and the spacing, this is

$$\left(y'_{ps_i}\right)_{ns} = \sum_{i=n}^{N} \left(y'_{ps_{i-1}}\right)_{ns} + \Delta y \qquad (29)$$

Because the normal shock is a straight line in the local frame of reference, all the integrations points have a local-axial coordinate equals to that from the transition point.

Knowing the integration-point coordinates for both, bow-wave portion and normal shock, the relative Mach number and relative flow angle for the first-captured wave are calculated as a Prandtl-Meyer expansion from the upstream conditions at every

integration point [1,28,29,31,35,36]. The first-captured wave is the first expansion wave that the inlet flow encounters as it approaches towards the blade. The first-captured wave extends from a point A on the adjacent blade suction surface to the intersecting point B between the stagnation streamline and the bow shock, namely the hyperbola vertex [28].

As the first-captured wave impingement point on the adjacent suction surface is unknown, a secant iteration method was implemented to obtain an accurate solution for the relative Mach number and relative flow angle on the wave E. The iterative approach assumes an axial location for the point A in the global frame of reference. Given z_A, a cubic-spline interpolation on the adjacent blade suction surface coordinates resolves y_A. Correspondingly, the blade suction surface angle β_{SS_A} at point A is obtained from a cubic-spline interpolation on the suction surface angles previously obtained from the conical blade-element layout method [20,21,37]. For the B-point, its absolute coordinates are equal to those from the bow-wave vertex, z_v and y_v.

The Riemman's equation between the upstream conditions and the right-running first-captured wave E is

$$\beta_1 + \nu_1(M_1') = \beta_E + \nu_E(M_E') \tag{30}$$

The first-captured flow angle at point A is equal to the wall suction surface angle β_{SS_A} at that point. Because the flow characteristics are conserved along a characteristic,

$$\beta_E = \beta_{SS_A} \tag{31}$$

Therefore, the first-captured wave Prandtl-Meyer angle is

$$\nu_E(M_E') = \beta_1 + \nu_1(M_1') - \beta_{SS_A} \tag{32}$$

Given the wave E Prandtl-Meyer angle, the Mach number is computed through a secant iteration method. From an asummed Mach number, the Prandtl-Meyer angle is obtained using the Prandtl-Meyer function. Thus, the error function E becomes

$$E = \nu_E(M_E') - \tilde{\nu}(\widetilde{M_E'}) \tag{33}$$

The same procedure repeats for a second assumed Mach number value. Having two assumed Mach numbers and two error values respectively, a straight line equation approximates the next estimated Mach number with an error of 0. The same scheme iteratively repeats until the error is less than a tolerance set of 1e-6 to find M_E'. Given M_E', the Mach angle μ_E is

$$\mu_E = \text{asin}(\frac{1}{M_E'}) \tag{34}$$

The first-captured wave is a straight line having a constante slope Σ_{ab} at every point on the wave:

$$\Sigma_{ab} = \frac{y_A - y_{ps_i}'}{z_A - z_{ps_i}'} \tag{35}$$

Inasmuch as a characteristic slope angle is the difference or sum of its flow angle and Mach angle, the right-running firs-captured wave slope turns

$$\Sigma_{ab} = \tan(\beta_E + \mu_E) = \frac{y_A - \widetilde{y_{ps_i}'}}{z_A - z_{ps_i}'} \tag{36}$$

Thus, $\widetilde{y_{ps_i}'}$ is solved from Eq. 36). As the overall estimation of the Prandtl-Meyer expansion is based on an assumed point-A axial location, the obtained y_{ps_i}' from Eq. 36) should be equal to the y_{ps_i}' given by the spacing in Eq. 27. For this, the error function becomes

$$E = \widetilde{y_{ps_i}'} - y_{ps_i}' \tag{37}$$

A secant iteration method is used to bring the error within a tolerance of 1e-6, and obtain well-estimated values for M_E' and β_E.

Thence, the shock angle for the passage bow-wave section at its corresponding integration points is given by

$$\left(\varsigma_{ps_i}\right)_{bow} = \varsigma_i - \beta_1 + \beta_E \tag{38}$$

Upon the passage normal-shock, the shock angle is expressed as

$$\left(\varsigma_{ps_i}\right)_{ns} = \frac{\pi}{2} - \beta_1 + \beta_E \tag{39}$$

Knowing the conditions upstream of the passage shock at state E, the pressure ratios and Mach numbers downstream at state 2 of it can be obtained for every passage-shock section. The relative total-pressure recovery across the passage shock is determined by the corresponding shock angle [27] at every integration point as in Eq. 19, becoming

$$\Pi'_{ps_i} = \left(\frac{P'_E}{P'_2}\right)_i$$

$$= \left[\frac{(\gamma + 1)M'_{E_i}{}^2 \sin^2 \varsigma_{ps_i}}{(\gamma - 1)M'_{E_i}{}^2 \sin^2 \varsigma_{ps_i} + 2}\right]^{\frac{\gamma}{\gamma-1}} \left[\frac{(\gamma + 1)}{2\gamma M'_{E_i}{}^2 \sin^2 \varsigma_{ps_i} - (\gamma - 1)}\right]^{\frac{1}{\gamma-1}} \tag{40}$$

The computation of the mass-averaged value for Eq. 40 is performed to the integration of all the points across the defined domain [28,29,31,38], expressed as

$$\overline{\Pi'_{ps}} = \overline{\left(\frac{P'_E}{P'_2}\right)} = \frac{\int_{y'_{ps_0}}^{y'_{ps_N}} M'_{E_i}\left(1 + \frac{\gamma - 1}{2}M'_{E_i}\right)^{\frac{-\gamma}{\gamma-1}+\frac{1}{2}} \Pi'_{ps_i}\cos(\frac{\pi}{2} - \varsigma_{ps_i})ds}{\int_{y'_{ps_0}}^{y_t'} M'_{E_i}\left(1 + \frac{\gamma - 1}{2}M'_{E_i}\right)^{\frac{-\gamma}{\gamma-1}+\frac{1}{2}} \cos(\frac{\pi}{2} - \varsigma_{ps_i})ds} \tag{41}$$

2.2.5   Total-Shock Loss Coefficient

The total-shock relative total-pressure loss due to the bow shock and passage shock is a product of their losses, expressed as

$$\Pi'_{sh} = \overline{\left(\frac{P'_E}{P'_2}\right)} * \left(\frac{P'_d}{P'_1}\right)_{bow} = \overline{\Pi'_{ps}} * \Pi'_{bow} \tag{42}$$

For which the mass-averaged total-shock loss-associated coefficient ϖ_{ts} [25] is

$$\varpi_{sh} = \frac{1 - \Pi'_{sh}}{1 - (1 + \frac{\gamma - 1}{2}M_1'^2)^{\gamma/1-\gamma}} \tag{43}$$

Despite passage bow-wave pressure losses were not considered for the overall total-shock loss as their effect was considered in the continuity equation for the unique incidence calculation [39], Bloch *et al.* [28] included the bow-wave portion effect in the passage-shock model developed. It was demonstrated that the bow-wave pressure deficit caused in the passage shock is small but significant. Given Π'_{bow} from Eq. 24, the passage bow-wave-associated loss coefficient is defined as

$$\varpi_{bow} = \frac{P'_1 - P'_d}{P'_1 - p_1} \tag{44}$$

Then, the passage-shock loss coefficient is expressed as

$$\varpi_{ps} = \varpi_{sh} - \varpi_{bow} \tag{45}$$

2.3   Choking Conditions

When the outlet static pressure decreases, the inlet meridional velocity increases, resulting in a mass flow rise. For the blade passage to accommodate more mass flow, the flow angle, and thus the incidence reduce. Nevertheless, there is a minimum value for the incidence, as the flow reaches a maximum velocity within the passage, and no further flow acceleration can be accomplished. As no lower incidence value is possible, the inlet velocity triangle remains constant, fixing the mass flow. This maximum mass

flow case is known as choke condition, corresponding to a minimum or choking incidence. For this reason, a choking-evolution model was developed and implemented into the 2-D SLC axial-flow fan/compressor performance simulator [2,5,18] to identify the streamtube choking level.

2.3.1   Choking Incidence

As the inlet relative Mach number increases, the ϖ vs i curve narrows, displacing to the right and upwards. This curve translation means that the minimum-loss increases and its corresponding incidences are higher for an inlet relative Mach number increment. The curve narrowing is explained as the incidence working range reduces when the inlet relative Mach number is raised, shortening the low-loss working range. The low-loss working range for choke operation is designated as [40]

$$R_{ch} = \alpha^* - \alpha_{nst} = i^* - i_{ch} \tag{46}$$

Where α is the angle for attack, and the subscripts $*$ and nst account for the design and negative-stall condition, respectively. The corresponding angles of attack calculation is based in a systematic methodology for 2-D NACA 65-series cascade tests [41], described in Aungier [40] and implemented in the 2-D SLC code by Pachidis [2].

An equivalent stall low-loss working range can be also defined as $(i_{st} - i^*)$. For low-speed cascades both low-loss working ranges, choke and stall decrease at the same rate as the inlet relative Mach number increases [42]. In contrast, for high-speed blade profiles, the choke low-loss working range $(i^* - i_{ch})$ reduces faster than $(i_{st} - i^*)$ as the M_1' is increased. Thus, the choking incidence i_{ch} becomes a function of M_1' and R_c, expressed as [40]

$$i_{ch} = \frac{i^* - R_{ch}}{1 + 0.5M_1'^3} \tag{47}$$

Eq. 47 sets the lowest possible for the incidence for a cascade and no incidence value should be below it, as this is the operating condition where no further mass flow increase is possible.

2.3.2   Choking Margin

The choking incidence estimation allows the flow field calculation for the choke condition. The inlet choking relative flow angle for a rotor becomes

$$\beta_{1_{ch}} = i_{ch} + k_1 \tag{48}$$

Similarly, for a stator the choking absolute flow angle is,

$$\alpha_{1_{ch}} = i_{ch} + k_1 \tag{49}$$

Given $\beta_{1_{ch}}$ or $\alpha_{1_{ch}}$ for the identified choked streamlines, an inverse design scheme is implemented to obtain the flow conditions that satisfy the choking incidence. In choke condition, the inlet relative whirl velocity is conserved as the blade speed remains constant and the swirl or inlet absolute angle α_1 condition does not change, keeping the inlet absolute whirl velocity unaffected. In the particular case of no swirl ($\alpha_1 = 0$), the inlet relative whirl velocity is equals to the blade speed at a given streamline radius. Therefore, inlet meridional relative velocity for a rotor in choke condition becomes

$$V_{1_{ch}} = \frac{V_{\theta_1}}{\sin \beta_{1_{ch}}} \tag{50}$$

It follows, that the inlet meridional choking velocity is

$$V_{m_{1_{ch}}} = \sqrt{V_{1_{ch}}^2 - V_{\theta_1}^2} \tag{51}$$

Hence, the inlet meridional absolute choking velocity is expressed as

$$C_{1_{ch}} = \sqrt{C_{\theta_1}^2 + V_{m_{1_{ch}}}} \tag{52}$$

In the absence of a relative velocity triangle for a static components (stator, IGV, OGV), $C_{1_{ch}}$ is directly computed from the inlet absolute choking flow angle,

$$C_{1_{ch}} = \frac{C_{\theta_1}}{\sin \alpha_{1_{ch}}} \tag{53}$$

Knowing $C_{1_{ch}}$, the inlet static temperature $T_{1_{ch}}$ and inlet specific ratio $\gamma_{1_{ch}}$ for choking operations are calculated through a secant iteration method by comparing the calculated total temperature against the real total temperature through the adiabatic steady flow energy equation. Having $T_{1_{ch}}$, the inlet meridional relative Mach number is obtained for the rotor,

$$M'_{1_{ch}} = \frac{V_{1_{ch}}}{a_{1_{ch}}} = \frac{V_{1_{ch}}}{\sqrt{\gamma_{1_{ch}} R T_{1_{ch}}}} \tag{54}$$

For static components, the inlet meridional absolute Mach number becomes

$$M_{1_{ch}} = \frac{C_{1_{ch}}}{\sqrt{\gamma_{1_{ch}} R T_{1_{ch}}}} \tag{55}$$

Having the above calculated flow parameters for the choking operations, a comparison is needed to determine how far is the current flow field from the choke conditions. Such comparison is done through a choking margin ratio λ that satisfies mass flow continuity. For this, the flow function as a unique function of a Mach number is

$$F(M) = \frac{\gamma}{\sqrt{\gamma - 1}} M \left[1 + \frac{\gamma - 1}{2} M^2 \right]^{\frac{-(\gamma+1)}{2(\gamma-1)}} \tag{56}$$

The flow function can be defined as well as the corrected mass flow per unit area,

$$F(M) = \frac{\dot{m}\sqrt{C_p T_0}}{A P_0} \tag{57}$$

Where A is the blade-throat area given by $s \cos \beta$

As mass flow continuity is satisfied between the upstream domain and a potentially choked blade inlet, it is valid to establish mass flow continuity between the current-flow and choke conditions,

$$\dot{m} = \dot{m}_{ch} \tag{58}$$

Substituting Eq. 56 and Eq. 57 in Eq. 58, mass flow continuity in a rotor becomes

$$\frac{F(M'_1) s \cos \beta_1 P_{01}}{\sqrt{C_p T_{01}}} = \frac{F(M'_{1_{ch}}) s \cos \beta_{1_{ch}} P_{01_{ch}}}{\sqrt{C_{p_{ch}} T_{01_{ch}}}} \tag{59}$$

In the case of static components, the mass flow continuity is expressed as

$$\frac{F(M_1) s \cos \alpha_1 P_{01}}{\sqrt{C_p T_{01}}} = \frac{F(M_{1_{ch}}) s \cos \alpha_{1_{ch}} P_{01_{ch}}}{\sqrt{C_{p_{ch}} T_{01_{ch}}}} \tag{60}$$

Between the immediate upstream domain and the blade inlet angle, the inlet total-temperature and inlet total-temperature are the same, and the specific heat ratio at constant pressure remains approximately constant, simplifying Eq. 60. Whereupon, a ratio between the actual and choking conditions from the simplified version of Eq. 60 defines the choking margin λ as follows

Rotor
$$\lambda = \frac{F(M'_1)}{F(M'_{1_{ch}})} \frac{\cos \beta_1}{\cos \beta_{1_{ch}}} \tag{61}$$

Stator,
IGV,OGV
$$\lambda = \frac{F(M_1)}{F(M_{1_{ch}})} \frac{\cos \alpha_1}{\cos \alpha_{1_{ch}}} \tag{62}$$

It is evident from Eq. 61 and Eq. 62 that if the inlet flow angle is lower than the inlet choking flow angle, the choking margin is greater than one, resulting in a choked blade passage.

3.0   RESULTS & DISCUSSION

3.1   Shock-Wave Structure

To validate the shock-pattern model, a 2-D SLC run was performed for the NASA Rotor 67. The validation of the shock data was done against charts as function of the inlet relative Mach number presented by Moeckel [24] and Miller and Hartmann [27].

A comparison of $\varsigma_{detach}, \varsigma_S, \varsigma_C$ against Moeckel's [24] reported values as a function of M_1', is displayed in Fig. 8 a), with a maximum difference of 0.12%. Similarly, the ratio of X'/y_{SB} and y_S/y_{SB} or non-dimensional detachment distance and sonic point height as a function of M_1' are compared in Fig. 8 b). The y_S/y_{SB} ratio is found to compare fairly reasonable with a maximum error of 0.35% for the highest Mach numbers and a maximum difference of 1.1% for the X'/y_{SB} ratio, due to the two scattered points observed. Apart from this marked difference, a maximum difference of 0.62% is found at the highest Mach number. One can note that for high Mach numbers, the detachment distance and the height of the sonic point are too small, resulting in close bow waves to the leading edge. As the inlet relative Mach number is decreased, the curves tend to infinity, leading in highly-detached bow waves.
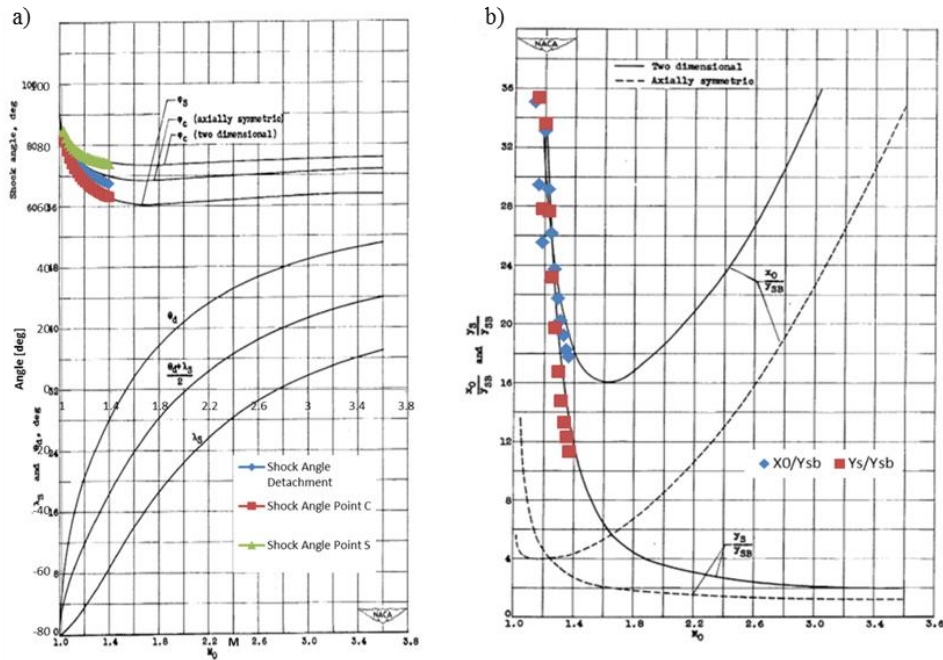

Figure 8 Bow-wave parameters comparison against chart presented by Moeckel [24] as a function of the inlet relative Mach number. a) Shock angles. b) Non-dimensional detachment distance and non-dimensional sonic point height.

Local-axial distance L between the sonic point and the bow-wave vertex is typically found as a ratio with respect of the point SB, which is the point that forms the wedge tangency. Fig. 9 shows the comparison of L/y_{SB} as a function of the inlet Mach number against a corresponding chart obtained by Miller and Hartmann [27]. The L/y_{SB} ratios estimated by the 2-D SLC fall around the curve, with a maximum difference of 1.7% and a minimum of 0.43%.
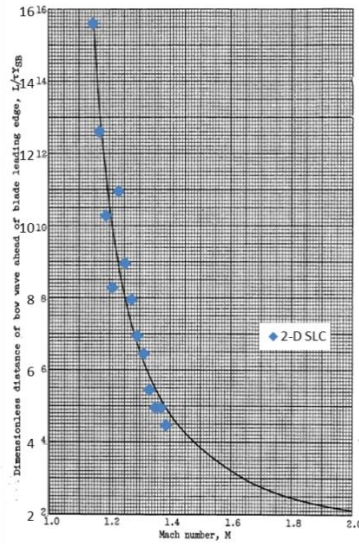
Figure 9 Comparison for the bow-wave non-dimensional distance from the wedge tangency point as a function of the inlet relative Mach number against chart presented by Miller and Hartmann [27].

3.2   Mass Flow Redistribution in Choking Conditions

The choking prediction model implemented in the 2-D SLC model, obtains a choking incidence for the whole blade span, which is the minimum value that the incidence for a given inlet Mach number. Fig. 10 shows the evolution of the current-flow and choking incidence values as a function of the outlet static pressure for the well-known NASA Rotor 67 [34]. It can be observed from left to right that the current-flow incidence is lower than the choking incidence limit at high-span locations. When this is the case, choke condition should be established for those stream tubes. As the back static pressure is increased, the blade span starts to unchoke.
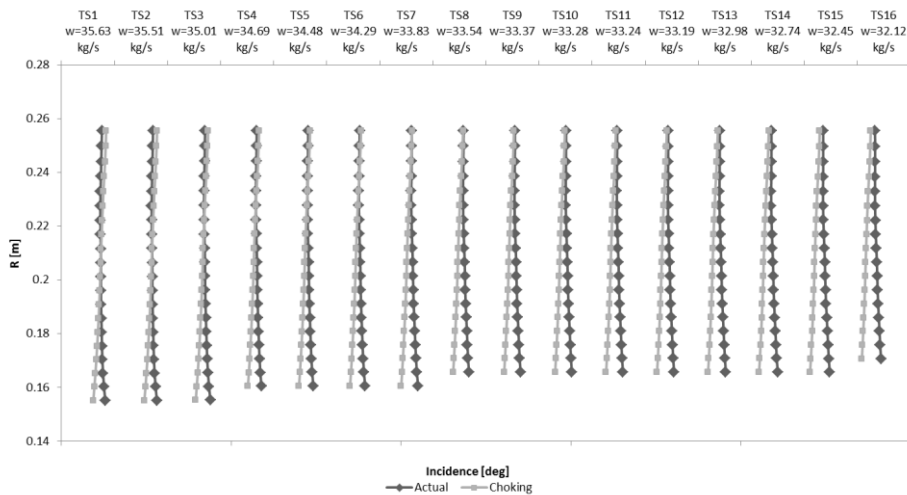

Figure 10 2-D SLC-estimated incidence and choking incidence evolution for the NASA Rotor 67 speedline at 100% NRT.

By compiling all the curves from Fig. 10 in Fig. 11, it is noted that the choking incidence limit does not significantly change across the off-design points, as it is more a function of the blade throat area and the inlet relative Mach number. Conversely, the current incidence grows faster than the choking incidence with the outlet static pressure. It is evident that the incidences that are on the left-hand side of the choking curve need to be limited to adopt the choking incidence value. Similarly, the compilation of inlet flow angle distributions from Fig. 12, results in an almost constant value for the inlet choking flow angle.
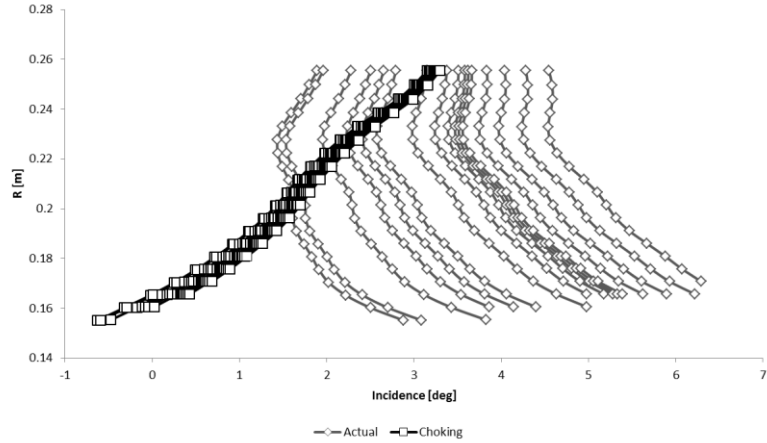
Figure 11 2-D SLC-estimated incidence and choking incidence for the NASA Rotor 67 at 100% NRT.
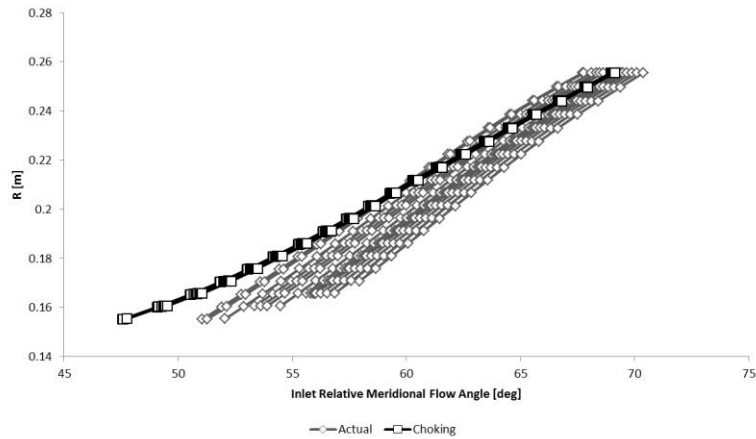

Figure 12 2-D SLC-estimated inlet flow angle and inlet choking flow angle for the NASA Rotor 67 at 100% NRT.

4.0   CONCLUSIONS

Modern aircraft gas turbine engines demand to be light and compact whilst being highly efficient. Transonic axial-flow compressors respond to these needs due to the additional loading caused by the passage shocks at the expense of an over-all shock loss increment. It has been acknowledged that 3-D CFD RANS tools are expensive and lack of flexibility. In contrast, 2-D SLC tools provide fast and reasonably accurate solution.

Transonic flow analysis is complex due to the shock structures involved and the associated phenomena.   When it comes to model transonic flow in 2-D SLC simulations, the aerodynamic performance solution can deviate from the actual conditions. For this reason, a 3-D blade-element-layout method, a shock- structure and loss model, and a novel choked mass flow redistribution scheme, were developed and implemented into an existing in-house 2-D SLC compressor performance code.

The shock model works in two parts: bow-wave structure and losses, and passage-shock structure and losses. The shock model was validated against NACA charts obtaining differences ~1%. The choking scheme predicts the choking, establishing a choking margin to determine the status of the current flow conditions from the choke operations. Given this, it is envisaged to limit the streamtube mass flow through a numerical approach depending on the choking margin level and is then redistributed from the blade tip regions to the low-span locations. The described improvements implemented in the 2-D SLC compressor performance simulator make the tool ready to

handle transonic flow with higher fidelity to be used not only in analysis mode, but also in paramount design optimisations.

REFERENCES

1.   Boyer KM. An Improved Streamline Curvature Approach for Off-Design Analysis of Transonic Axial Compression Systems. PhD Thesis. Virginia Polythenic Institute and State University, Blacksburg, Virginia, United States of America; 2001. pp. 1–168.

2.   Pachidis V. Gas Turbine Advanced Performance Simulation. PhD Thesis. Cranfield University, School of Engineering, Cranfield, United Kingdom; 2006. pp. 1–384.

3.   Denton JD., Dawes WN. Computational Fluid Dynamics for Turbomachinery Design. Proceedings IMechE Part C: J. Mechanical Engineering Science. 1998; 213(2): 107–124.

4.   Denton JD. Some Limitations of Turbomachinery CFD. ASME Turbo Expo 2010: Power for Land, Sea and Air. 14-18 June, Glasglow, United Kingdom: GT2010-22540; 2010. pp. 1–11.

5.   Pachidis V., Pilidis P., Marinai L., Templalexis I. Towards a Full Two Dimensional Gas Turbine Performance Simulator. Aeronautical J. 2007; 111(1121): 433–442.

6.   Pachidis V., Pilidis P., Templalexis I., Alexander T., Kotsiopoulos P. Prediction of Engine Performance Under Compressor Inlet Flow Distortion Using Streamline Curvature. ASME Turbo Expo 2006: Power for Land, Sea and Air. 8-11 May, Barcelona, Spain: GT2006-90806; 2006. pp. 1–17.

7.   Pachidis V., Pilidis P., Templalexis I., Korakianitis T., Kotsiopoulos P. Prediction of Engine Performance Under Compressor Inlet Flow Distortion Using Streamline Curvature. ASME J. Engineering for Gas Turbines and Power. 2007; 129(1): 97–103.

8.   Templalexis I., Pilidis P., Pachidis V., Kotsiopoulos P. Development of a Two-Dimensional Streamline Curvature Code. ASME J. Turbomachinery. 2011; 133(1): 1–7.

9.   Smith Jr. LH. The Radial-Equilibrium Equation of Turbomachinery. Trans. ASME J. Engineering for Power. 1966; 88(1): 1–12.

10.   Marsh H. A digital computer program for the through-flow fluid mechanics in an arbitrary turbomachine using a matrix method. Aeronautical Research Council Reports and Memoranda. Ministry of Technology, London, United Kingdom: R. & M. No. 3509; 1968. pp. 1–34.

11.   Tiwari P., Stein A., Lin Y-L. Dual-Solution and Choked Flow Treatment in a Streamline Curvature Throughflow Solver. ASME J. Turbomachinery. 2013; 135(4): 1–11.

12.   Sayari N., Bolcs A. A New Throughflow Approach For Transonic Axial Compressor Stage Analysis. ASME 1995 Int. Gas Turbine and Aeroengine Congress and Exposition. 5-8 June, Houston, Texas, United States of America: 95-GT-195; 1995. pp. 1–12.

13.   Reed JA., Afjeh AA. Development of a Protoype Simulation Executive with Zooming in the Numerical Propulsion System Simulation. NASA Contract Report. University of Toledo, Mechanical Engineering Deparment, Toledo, Ohio, United States of America: NASA CR-200613; 1995. pp. 1–66.

14.   Reed JA., Turner MG., Norris A., Veres JP. Towards an Automated Full-

Turbofan Engine Numerical Simulation. NASA Technical Memorandum; XVI Int. Symposium on Air Breathing Engines 2003. Glenn Research Center, Cleveland, Ohio, United States of America; 31 August-5 September, Cleveland, Ohio, United States of America: NASA/TM-2003-212494; 2003. pp. 1–16.

15.   Turner MG., Reed JA., Ryder R., Veres JP. Multi-Fidelity Simulation of a Turbofan Engine With Results Zoomed Into Mini-Maps for a Zero-D Cycle Simulation. NASA Technical Memorandum; ASME Turbo Expo 2004: Power for Land, Sea and Air. Glenn Research Center, Cleveland, Ohio, United States of America; 14-17 June, Vienna, Austria: NASA TM-2004-213076; GT2004-53956; 2004. pp. 1–18.

16.   Pachidis V., Pilidis P., Talhouarn F., Kalfas A., Templalexis I. A Fully Integrated Approach to Component Zooming Using Computational Fluid Dynamics. ASME J. Engineering for Gas Turbines and Power. 2006; 128(3): 579–584.

17.   Pachidis V., Pilidis P., Texeira J., Templalexis I. A comparison of component zooming simulation strategies using streamline curvature. Proceedings IMechE Part G: J. Aerospace Engineering. 2006; 221(5): 1–15.

18.   Templalexis I., Pilidis P., Pachidis V., Kotsiopoulos P. Development of a 2-D Compressor Streamline Curvature Code. ASME Turbo Expo 2006: Power for Land, Sea and Air. 8-11 May, Barcelona, Spain: GT2006-90867; 2006. pp. 1–10.

19.   Adamczyk JJ. Aerodynamic Analysis of Multistage Turbomachinery Flows in Support of Aerodynamic Design. ASME Int. Gas Turbine & Aeroengine Congress & Exhibition. 7-10 July, Indianapolis, Indiana, United States of America: PP-GT-80; 1999. pp. 1–40.

20.   Crouse JE., Junetzke DC., Schwirian RE. A Computer Program for Composing Compressor Blading from Simulated Circular-Arc Elements on Conical Surfaces. NASA Technical Note. Lewis Research Center, Cleveland, Ohio, United States of America: NASA TN D-5437; 1969. pp. 1–82.

21.   Crouse JE., Gorrell WT. Computer Program for Aerodynamic and Blading Design of Multistage Axial-Flow Compressors. NASA Technical Paper. Lewis Research Center, Cleveland, Ohio, United States of America: NASA TP-1946; AVRADCOM TR 80-C-21; 1981. pp. 1–101.

22.   Prince Jr. DC. Three-Dimensional Shock Structures for Transonic/Supersonic Compressor Rotors. AIAA J. Of Aircraft. 1980; 17(1): 28–37.

23.   Chang H., Zhu F., Jin D., Gui X. Effect of Blade Sweep on Inlet Flow in Axial Compressor Cascades. Chinese J. Aeronautics. 2015; 28(1): 103–111.

24.   Moeckel WE. Approximate Method for Predicting Form and Location of Detached Shock Waves Ahead of Plane or Axially Symmetric Bodies. NACA Technical Note. Lewis Flight Propulsion Laboratory, Cleveland, Ohio, United States of America: NACA TN 1921; 1949. pp. 1–32.

25.   Lewis GW., Tysl ER., Fessler TE. Analysis of Transonic Rotor-Blade Passage Loss with Hot-Wire Anemometers. Research Memorandum. Lewis Flight Propulsion Laboratory, Cleveland, Ohio, United States of America: NACA RM E58C04; 1958. pp. 1–28.

26.   Schwenk FC., Lewis GW., Hartmann MJ. A Preliminary Analysis of the Magnitude of Shock Losses in Transonic Compressors. Research Memorandum. Lewis Flight Propulsion Laboratory, Cleveland, Ohio, United States of America: NACA RM E57A30; 1957. pp. 1–49.

27.   Miller GR., Hartmann MJ. Experimental Shock Configurations and Shock Losses in a Transonic-Compressor Rotor at Design Speed. NACA Research

Memorandum. Washington, D.C., United States of America: RM E58A14b; 1958. pp. 1–55.

28. Bloch GS., Copenhaver WW., O'Brien WF. A Shock Loss Model for Supersonic Compressor Cascades. Trans. ASME J. Turbomachinery. 1999; 121(1): 28–35.

29. Boyer KM., O'Brien WF. An Improved Streamline Curvature Approach for Off-Design Analysis of Transonic Axial Compression Systems. Trans. ASME J. Turbomachinery. 2003; 125(3): 475–481.

30. Boyer KM., O'Brien WF. An Improved Streamline Curvature Approach for Off-Design Analysis of Transonic Axial Compression Systems. thesis. 2003; 125(April): 475.

31. Boyer KM., O'Brien WF. Application of an Improved Streamline Curvature Approach to a Modern, Two-Stage, Transonic Fan: Comparison with Data and CFD. ASME Turbo Expo 2002. 3-6 June, Amsterdam, The Netherlands: GT-2002-30383; 2002. pp. 1–10.

32. Klapproth JF. Approximate Relative-Total-Pressure Losses of an Infinite Cascade of Supersonic Blades with Finite Leading-Edge Thickness. NACA Research Memorandum. Washington, D.C., United States of America: NACA RM E9L21; 1950.

33. Miller GR., Lewis Jr. GW., Hartmann MJ. Shock Losses in Transonic Compressor Blade Rows. Trans. ASME J. Engineering for Power. 1961; 60(WA-77): 1–7.

34. Strazisar AJ., Wood JR., Hathaway MD., Suder KL. Laser Anemometer Measurements in a Transonic Axial-Flow Fan Rotor. NASA Technical Paper. Lewis Research Center, Cleveland, Ohio, United States of America: NASA TP-2879; 1989. pp. 1–214.

35. Schobeiri MT. Advanced Compressor Loss Correlations, Part I: Theoretical Aspects. Int. J. Rotating Machinery. 1997; 3(3): 163–177.

36. Schobeiri MT. Advanced Compressor Loss Correlations, Part II: Experimental Verifications. Int. J. Rotating Machinery. 1997; 3(3): 179–187.

37. Azamar Aguirre H. Transonic Axial-Flow Compressor Design, Performance Simulation and Optimization. 9th Month Review Assesment. 2015. pp. 1–127.

38. Boyer KM., O'Brien WF. An Improved Streamline Curvature Approach for Off-Design Analysis of Transonic Axial Compression Systems. Thesis. 2003; 125(April): 475.

39. Starken H., Yongxing Z., Schreiber H-A. Mass Flow Limitation of Supersonic Blade Rows due to Leading Edge Blockage. ASME 1984 Int. Gas Turbine Conference and Exhibit. 4-7 June, Amsterdam, The Netherlands: 84-GT-233; 1984. pp. 1–7.

40. Aungier RH. Axial-Flow Compressors. 1st edn. New York, New Yor, United States of America: ASME Press; 2003. 368 p.

41. Herrig JL., Emery JC., Erwin JR. Systematic Two-Dimensional Cascade Tests of Naca 65-Series Compressor Blades at Low Speeds. NACA Technical Note. Langley Aeronautical Laboratory, Langley Field, Virginia, United States of America: NACA TN 3916; 1957. p. 226.

42. Johnsen IA., Bullock RO. Aerodynamic Design of Axial-Flow Compressors. NASA Single Research Memorandum Volume. Lewis Research Center, Cleveland, Ohio, United States of America: NASA SP-36; 1965. pp. 1–508.